Numerical modeling of acoustic emission in laminated tensile test specimens

Mats Åberg *

Department of Solid Mechanics, Royal Institute of Technology, KTH, 100 44 Stockholm, Sweden

Received 1 September 1999

Abstract

Acoustic emission from transverse matrix cracks and fiber fracture in typical laminated tensile test specimens is modeled. The acoustic sources are described as time dependent displacement discontinuities which subsequently are translated to volume forces. The transient waves are computed using a finite element model of the specimen's cross-section. The finite element modeling leads to a system of differential equations in the axial coordinate and time. The differential equations are solved using Fourier transforms and eigenmode superposition followed by inversion of the transforms through residue calculus and FFT. Computed time histories for matrix cracking and fiber fracture are presented. The highest frequency content in these signals corresponds typically to 300 kHz. A method to measure the average matrix crack propagation velocity is suggested. © 2001 Elsevier Science Ltd. All rights reserved.

Keywords: Numerical modeling; Acoustic emission; FFT

1. Introduction

Final failure of composite laminate components is often preceded by significant damage of the material in the component, for example by matrix cracking, fiber fracture and delamination. Understanding and modeling of the damage processes are valuable tools in integrity assessment and design of such components. A special feature of material degradation in polymer based composites, as opposed to metals, is that the damage events are often very localized in space and time, and the physical dimensions of the damage are often larger than in metals. This means that each damage event will produce a distinct stress pulse in the specimen. Measuring the stress pulse, i.e. the acoustic emission (AE), is therefore a good way of monitoring damage evolution experiments on composite materials.

The recent development in electronics has made it possible to record and store AE signals. Models of the AE chain, from source to recorded signal, can then be used to identify and quantify the damage event – so-called quantitative acoustic emission. A review on quantitative AE is presented by Scruby (1985), and examples of use on composite materials can be found in the works by Gorman and Ziola (1991), Prosser et al. (1995) and Qi et al. (1997).

---

* Fax: +46-8-55383310.
E-mail address: mats.aberg@scania.com (M. Åberg).

Modeling of the AE-chain can be divided into four basic parts. Modeling of damage (or source), wave propagation from source to receiver, receiver response due to surface movement on the specimen and modeling of the recording system behind the receiver, which often includes some wanted and unwanted filtering. This work will be concerned with the first two aspects, that is source modeling and wave propagation.

Burridge and Knopoff (1964) have shown that displacement discontinuities, or cracks, can be replaced by equivalent volume forces, giving rise to the same wave field in the body. The volume forces and their distribution can be summarized in a so-called moment tensor, provided that the dimensions of the displacement discontinuity are much smaller than the dimensions of the body and the smallest wavelength studied, see the work of Rice (1980). The moment tensor has been used extensively to analyze acoustic emission in different materials and geometries, for example by Chang and Sachse (1986), Guo et al. (1996), Landis and Shah (1993) and Ohtsu (1995).

Wave propagation in elastic waveguides has been studied for more than 100 years, and the arsenal of methods is substantial, see for example the books by Graff (1991) and Miklowitz (1984). The well-known analytical solutions for wave propagation in homogeneous isotropic plates and rods due to Lamb and Pochhammer respectively may also be found in these books.

Anisotropic and inhomogeneous elastic waveguides, especially plates, have also been studied. A commonly employed technique for plates is to use integral transforms in time and the in-plane coordinates. The equation describing motion in the vertical direction is then solved analytically or numerically. The subsequent inversion of the in-plane coordinate transforms is often done using contour integration, evaluated using residues, or by direct numerical integration. A good survey of the subject can be found in the introduction of the work by Weaver et al. (1996).

Analysis of AE in large composite plates can also be done using approximate plate theories, such as the Reissner–Mindlin plate theory, see Guo et al. (1996). The plate theory is usually valid in the frequency range of interest and the distance between the source and the receiver is often several plate thicknesses. Experiments on large composite panels are, however, expensive and unpractical. In tensile test specimens the distance between receiver and source is often of same order as the width of the specimen, and the use of plate methods in this case is complicated by the boundaries in the width direction, see Liu et al. (1990). This is especially true for broad band sources.

An alternative to plate theory is a beam model. Åberg and Gudmundson (1999) have used a higher order beam model to study wave propagation due to AE in tensile test specimen. It was, however, found that the beam model, although it included the lowest optical mode, had a range of validity in frequency which was too small. For typical test specimens the maximum frequency was 50 kHz whereas important AE frequencies are up to 10 times higher (de Groot et al., 1995). In deriving the beam model a displacement field for the whole cross-section was assumed, but another way to describe the displacement field is to divide the cross-section into finite elements. This leads to an eigenvalue problem with frequencies or wave numbers as eigenvalues or parameters, and the eigenvectors describe the displacements. Aalami (1973) and Talbot and Przemieniecki (1975) were among the first to use this approach to compute dispersion relations and eigenmodes for waveguides with homogeneous cross-sections. Volovoi et al. (1998) have done the same for inhomogeneous rectangular cross-sections, and Huang and Dong (1984) for laminated circular cross-sections. Transient axisymmetrical motion in laminated circular tubes has been studied by Kohl et al. (1992a,b) using superposition of eigenmodes. Dispersion relations for propagating modes can also be computed using standard finite element codes as described by Åberg and Gudmundson (1997).

In this work, transient wave motion in laminated tensile test specimens due to transverse matrix cracking and fiber fracture is computed. The fiber fracture is modeled using a time dependent volume force, and matrix cracking is described by a volume force depending on both position and time. Wave propagation is modeled by dividing the cross-section into finite elements, leading to a system of ordinary differential equations in the nodal displacements, which are functions of the axial coordinate and time. The system is

solved using Fourier transforms, and the solution of the resulting algebraic problem is written as a su-perposition of eigenmodes. Contour integration, using residue calculus, and FFT are used to invert the transforms.

2. Source modeling

The modeling presented in this section is identical to the modeling in Åberg and Gudmundson (1999) and is presented here for clarity reasons. A laminate and a Cartesian coordinate system according to Fig. 1 is considered. The laminate is made of transversely isotropic plies. It is infinite in the 1-direction and bounded by free surfaces at $x_2 = \pm b$ and $x_3 = \pm h$. In modeling the sources, it is for simplicity assumed that the damage occurs in plies with the symmetry directions along the 1- or 2-direction respectively (0°- and 90°-plies).

2.1. Matrix cracking

If the laminate under consideration is strained in the 1-direction, the first damage that typically appears is matrix cracking in the 90°-layers. It is often, if not always, found that the cracks will initiate at one of the edges and then propagate across the width of the specimen or stop within it, Prosser et al. (1995).

Consider a matrix crack at $x_1 = 0$ growing in the 2-direction. In the proceeding analysis, only wave-lengths which are several ply thicknesses long will be considered. For a dynamically growing matrix crack, it can be assumed that a steady state crack opening will develop at a distance of the order of a few ply thicknesses behind the crack tip. Thus, if short wavelength information in the solution is ignored, the crack-opening displacement in the 1-direction may be expressed as

$$\Delta u_1(x_2, x_3, t) = \Delta u^{\text{stat}}(x_3) J_{\text{m}}(x_2, t), \tag{1}$$

where Δu^{stat} is the static crack-opening displacement of a crack in a laminate of infinite width subjected to the same strain in the 1-direction and to generalized plane strain in the 2-direction. The function J_{m} may within the same order of long wavelength approximation be expressed as
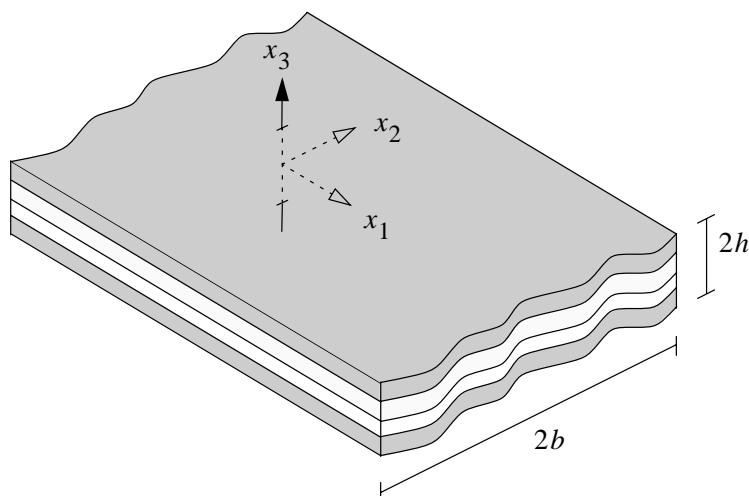

Fig. 1. Definition of coordinate system and geometry of the laminated specimen.

$$J_{\mathrm{m}}(x_2, t) = \begin{cases} 0 & t < 0, \\ H(-x_2 - b + vt) & t \geqslant 0, \end{cases} \tag{2}$$

where H is the Heaviside step function. On a global scale it is a reasonable model of a crack growing across the entire width of the laminate with an average velocity, v. The crack-opening displacement may alternatively be viewed as a displacement discontinuity in the 1-direction. Using the work by Burridge and Knopoff (1964), it can be expressed by equivalent volume forces, f_i. The result in this case is

$$f_i = -C_{11ij}^{\mathrm{T}} \frac{\partial}{\partial x_j} [J_{\mathrm{m}}(x_2, t) \Delta u^{\mathrm{stat}}(x_3) \delta(x_1)], \tag{3}$$

where δ is the Dirac delta function and C_{ijkl}^{T} is the stiffness tensor of the 90°-ply containing the crack. The function Δu^{stat} has to be known in order to evaluate the expression in Eq. (3). One possible method is to perform finite element computations on a two-dimensional plane-strain model representing the cracked laminate and then fit an appropriate function to the resulting crack opening. Here an alternative method will be used.

Gudmundson and Zang (1993) have proposed a method to compute the stiffness loss of a composite laminate containing matrix cracks. This is based on the assumption that the crack opening is mainly influenced by the state in the cracked ply, and that the rest of the plies have negligible direct influence on the crack opening. This method has been found to yield very good stiffness-loss estimations, Adolfsson and Gudmundson (1995). Bearing this in mind, the opening of an internal matrix crack can be approximated using the opening of a crack in an infinite plate under plane strain, and the opening of a surface crack can be approximated by the opening of an edge crack in a semi-infinite plate under plane strain. Expressions for these crack openings may be found in the book by Wu and Carlsson (1991). Please note that, within the scope of the approximation, the anisotropy of the plies presents no problem since the material is isotropic in the plane of the crack. Once Δu^{stat} is known, the volume forces according to Eq. (3) can be calculated.

2.2. Fiber fracture

Further straining of the specimen will among other types of damage cause fiber fracture. Whereas matrix cracking is hardly localized to a point in a uniaxial test, fiber fracture approximately is. Here a fiber fracture located at $x_1 = 0$, $x_2 = b_{\mathrm{f}}$ and $x_3 = h_{\mathrm{f}}$ within a 0°-ply is considered. The volume force is expressed as

$$f_i = -\bar{u}^{\mathrm{stat}} J_{\mathrm{f}}(t) r^2 \pi C_{ij11}^{\mathrm{f}} \frac{\partial}{\partial x_j} [\delta(x_1) \delta(x_2 - b_{\mathrm{f}}) \delta(x_3 - h_{\mathrm{f}})], \tag{4}$$

where $\bar{u}^{\mathrm{stat}}$ is the average separation between the broken fiber ends under static loading, C_{ijkl}^{f} the stiffness tensor of the fiber and r the radius of the fiber. The time dependence is assumed to have the form

$$J_{\mathrm{f}}(t) = \begin{cases} t/\tau & 0 < t < \tau, \\ 1 & \tau < t. \end{cases} \tag{5}$$

This means that the average separation increases linearly to the static value during a time period of length τ.

The value of $\bar{u}^{\mathrm{stat}}$ can be estimated in different ways. Here, a simple estimate due to Cox will be used, see Gibson (1994). Using Cox's model and letting the fiber length approach infinity, the separation of the fiber ends becomes

$$\bar{u}^{\mathrm{stat}} = \bar{\varepsilon}_1 r \sqrt{\frac{E_{\mathrm{f}} \ln(1/V_{\mathrm{f}})}{G_{\mathrm{m}}}}, \tag{6}$$

where $\bar{\varepsilon}_1$ is the strain in the 1-direction of the ply, r the radius of the fiber, E_{f} the elastic modulus of the fiber, V_{f} the fiber volume fraction and G_{m} the shear modulus of the matrix material.

3. Wave propagation

Based on Eqs. (3) and (4) matrix cracking and fiber fracture may be represented by equivalent volume forces. Below the resulting wave propagation will be considered.

3.1. Finite element formulation

In order to calculate the wave motion, the cross-section is discretized into finite elements by assuming a displacement field according to

$$u_i(x_j, t) = \underset{\sim}{U}^{\mathrm{T}}{}_i(x_1, t)\varphi(x_2, x_3), \tag{7}$$

where, the superscript T denotes transpose, $\underset{\sim}{U}_i$ is a column vector with nodal displacements in the i-direction as its elements and φ is a column vector containing the basis functions φ_n.

The material in the cross-section is assumed to be elastic transversely isotropic with the 1-, 2- or 3-directions as symmetry directions. Thus, the constitutive relation can be expressed as

$$\begin{bmatrix} \sigma_{11} \\ \sigma_{22} \\ \sigma_{33} \\ \sigma_{23} \\ \sigma_{12} \\ \sigma_{13} \end{bmatrix} = \begin{bmatrix} c_{11} & c_{12} & c_{13} & 0 & 0 & 0 \\ c_{12} & c_{22} & c_{23} & 0 & 0 & 0 \\ c_{13} & c_{23} & c_{33} & 0 & 0 & 0 \\ 0 & 0 & 0 & c_{44} & 0 & 0 \\ 0 & 0 & 0 & 0 & c_{55} & 0 \\ 0 & 0 & 0 & 0 & 0 & c_{66} \end{bmatrix} \begin{bmatrix} \varepsilon_{11} \\ \varepsilon_{22} \\ \varepsilon_{33} \\ \gamma_{23} \\ \gamma_{12} \\ \gamma_{13} \end{bmatrix}, \tag{8}$$

using the usual notation for stresses and strains. Hamilton's principle is now used to derive differential equations for the nodal displacements $\underset{\sim}{U}_i$. Reflections from the ends of the specimen will not be treated in this work and therefore boundary conditions are not included. The resulting system of differential equations is

$$[K_{11}^{00}]\frac{\partial^2 \underset{\sim}{U}_1}{\partial x_1^2} + \left([K_{12}^{02}] - [K_{55}^{02}]^{\mathrm{T}}\right)\frac{\partial \underset{\sim}{U}_2}{\partial x_1} + \left([K_{13}^{03}] - [K_{66}^{03}]^{\mathrm{T}}\right)\frac{\partial \underset{\sim}{U}_3}{\partial x_1} - \left([K_{55}^{22}] + [K_{66}^{33}]\right)\underset{\sim}{U}_1 + \underset{\sim 1}{F}$$

$$= [M]\frac{\partial^2 \underset{\sim}{U}_1}{\partial t^2}, \tag{9}$$

$$[K_{55}^{00}]\frac{\partial^2 \underset{\sim}{U}_2}{\partial x_1^2} - \left([K_{12}^{02}]^{\mathrm{T}} - [K_{55}^{02}]\right)\frac{\partial \underset{\sim}{U}_1}{\partial x_1} - \left([K_{23}^{23}] + [K_{44}^{23}]^{\mathrm{T}}\right)\underset{\sim}{U}_3 - \left([K_{22}^{22}] + [K_{44}^{33}]\right)\underset{\sim}{U}_2 + \underset{\sim}{F}_2$$

$$= [M]\frac{\partial^2 \underset{\sim}{U}_2}{\partial t^2}, \tag{10}$$

$$[K_{66}^{00}]\frac{\partial^2 \underset{\sim}{U}_3}{\partial x_1^2} - \left([K_{13}^{03}]^{\mathrm{T}} - [K_{66}^{03}]\right)\frac{\partial \underset{\sim}{U}_1}{\partial x_1} - \left([K_{23}^{23}]^{\mathrm{T}} + [K_{44}^{23}]\right)\underset{\sim}{U}_2 - \left([K_{33}^{33}] + [K_{44}^{22}]\right)\underset{\sim}{U}_3 + \underset{\sim}{F}_3$$

$$= [M]\frac{\partial^2 \underset{\sim}{U}_3}{\partial t^2}, \tag{11}$$

where the matrices are defined by

$$\left[K_{ij}^{00}\right] = \int_{-b}^{b}\int_{-h}^{h} c_{ij}\underset{\sim}{\varphi}\underset{\sim}{\varphi}^{\mathrm{T}}\,\mathrm{d}x_3\,\mathrm{d}x_2, \qquad \left[K_{ij}^{nm}\right] = \int_{-b}^{b}\int_{-h}^{h} c_{ij}\frac{\partial \underset{\sim}{\varphi}}{\partial x_n}\frac{\partial \underset{\sim}{\varphi}^{\mathrm{T}}}{\partial x_m}\,\mathrm{d}x_3\,\mathrm{d}x_2, \tag{12}$$

$$\left[K_{ij}^{0n}\right] = \int_{-b}^{b} \int_{-h}^{h} c_{ij}\underset{\sim}{\varphi}\frac{\partial \underset{\sim}{\varphi}^{\mathrm{T}}}{\partial x_n}\,\mathrm{d}x_3\,\mathrm{d}x_2 \quad \text{and} \quad [M] = \int_{-b}^{b} \int_{-h}^{h} \rho\underset{\sim}{\varphi}\underset{\sim}{\varphi}^{\mathrm{T}}\,\mathrm{d}x_3\,\mathrm{d}x_2, \tag{13}$$

and ρ is the density. The force vectors, $\underset{\sim}{F}_i$, are derived from

$$\underset{\sim}{F}_i = \int_{-b}^{b} \int_{-h}^{h} f_i\underset{\sim}{\varphi}\,\mathrm{d}x_3\,\mathrm{d}x_2. \tag{14}$$

Please note, that the system of differential equations describe three-dimensional wave propagation and source excitation even if x_2 and x_3 do not appear explicitly in Eqs. (9)–(11) or in the proceeding solution.

3.2. Transformed solution

The system of differential equations given by Eqs. (9)–(11) are solved using the following Fourier transform pairs in time and space

$$\hat{\underset{\sim}{V}}(\xi,t) = \int_{-\infty}^{\infty} \underset{\sim}{V}(x_1,t)\mathrm{e}^{-\mathrm{i}x_1\xi}\,\mathrm{d}x_1, \qquad \underset{\sim}{V}(x_1,t) = \frac{1}{2\pi}\int_{-\infty}^{\infty} \hat{\underset{\sim}{V}}(\xi,t)\mathrm{e}^{\mathrm{i}x_1\xi}\,\mathrm{d}\xi, \tag{15}$$

$$\underset{\sim}{V}^*(x_1,\omega) = \int_{-\infty}^{\infty} \underset{\sim}{V}(x_1,t)\mathrm{e}^{\mathrm{i}\omega t}\,\mathrm{d}t, \qquad \underset{\sim}{V}(x_1,t) = \frac{1}{2\pi}\int_{-\infty}^{\infty} \underset{\sim}{V}^*(x_1,\omega)\mathrm{e}^{-\mathrm{i}\omega t}\,\mathrm{d}\omega. \tag{16}$$

Employing the transforms to the differential equations leads to a system of algebraic equations for the unknown transformed nodal displacements $\hat{Q}^*$,

$$\left(\xi^2[K_2] + \mathrm{i}\xi[K_1] + [K_0] - \omega^2[M_{\mathrm{Tot}}]\right)^* = \hat{\underset{\sim}{F}}^*, \tag{17}$$

where the vectors $\hat{Q}^*$ and $\hat{\underset{\sim}{F}}^*$ are

$$\hat{Q}^* = \begin{bmatrix} \hat{\underset{\sim}{U}}_1^* \\ \hat{\underset{\sim}{U}}_2^* \\ \hat{\underset{\sim}{U}}_3^* \end{bmatrix} \quad \text{and} \quad \hat{\underset{\sim}{F}}^* = \begin{bmatrix} \hat{\underset{\sim}{F}}_1^* \\ \hat{\underset{\sim}{F}}_2^* \\ \hat{\underset{\sim}{F}}_3^* \end{bmatrix}.$$

The symmetric matrices $[K_2]$, $[K_0]$ and $[M_{\mathrm{Tot}}]$ are defined by

$$[K_2] = \begin{bmatrix} \left[K_{11}^{00}\right] & [0] & [0] \\ [0] & \left[K_{55}^{00}\right] & [0] \\ [0] & [0] & \left[K_{66}^{00}\right] \end{bmatrix}, \qquad [M_{\mathrm{Tot}}] = \begin{bmatrix} [M] & [0] & [0] \\ [0] & [M] & [0] \\ [0] & [0] & [M] \end{bmatrix}, \tag{18}$$

$$[K_0] = \begin{bmatrix} \left[K_{55}^{22}\right] + \left[K_{66}^{33}\right] & [0] & [0] \\ [0] & \left[K_{22}^{22}\right] + \left[K_{44}^{33}\right] & \left[K_{44}^{23}\right]^{\mathrm{T}} + \left[K_{23}^{23}\right] \\ [0] & \left[K_{44}^{23}\right] + \left[K_{23}^{23}\right]^{\mathrm{T}} & \left[K_{33}^{33}\right] + \left[K_{44}^{22}\right] \end{bmatrix}, \tag{19}$$

and the antisymmetric matrix $[K_1]$ by

$$[K_1] = \begin{bmatrix} [0] & \left[K_{55}^{02}\right]^{\mathrm{T}} - \left[K_{12}^{02}\right] & \left[K_{66}^{03}\right]^{\mathrm{T}} - \left[K_{13}^{03}\right] \\ -\left(\left[K_{55}^{02}\right] - \left[K_{12}^{02}\right]^{\mathrm{T}}\right) & [0] & [0] \\ -\left(\left[K_{66}^{03}\right] - \left[K_{13}^{03}\right]^{\mathrm{T}}\right) & [0] & [0] \end{bmatrix}. \tag{20}$$

The homogeneous version of Eq. (17) defines an eigenvalue problem in ω^2 for a given ξ. Denote the eigenvalues $\omega_n^2(\xi)$ and the right and left eigenvectors by $\underset{\sim}{V}_n(\xi)$ and $\underset{\sim}{W}_n(\xi)$, respectively. The eigenvectors are normalized such that

$$\underset{\sim}{W}^{\mathrm{T}}_m [M_{\mathrm{Tot}}] \underset{\sim}{V}_n = \delta_{mn}, \tag{21}$$

hence

$$\underset{\sim}{W}^{\mathrm{T}}_n \big(\xi^2 [K_2] + \mathrm{i}\xi [K_1] + [K_0] \big) \underset{\sim}{V}_n = \omega_n^2, \tag{22}$$

where δ_{mn} is Kronecker's delta. Using relations (21) and (22), and Eq. (17) the solution $\hat{U}^*$ may be written as

$$\hat{U}^*(\xi, \omega) = \sum_{n=1}^{3N} \frac{\underset{\sim}{W}^{\mathrm{T}}_n(\xi) \hat{F}^*(\xi, \omega)}{\omega_n^2(\xi) - \omega^2} \underset{\sim}{V}_n(\xi), \tag{23}$$

N being the number of nodes in the cross-section.

3.3. Inverse Fourier transform

An inversion with respect to ξ is first considered. Eqs. (15) and (23) then give

$$\underset{\sim}{U}^*(x_1, \omega) = \frac{1}{2\pi} \sum_{n=1}^{3N} \int_{-\infty}^{\infty} \frac{\underset{\sim}{W}^{\mathrm{T}}_n(\xi) \hat{F}^*(\xi, \omega)}{\omega_n^2(\xi) - \omega^2} \underset{\sim}{V}_n(\xi) \mathrm{e}^{\mathrm{i}\xi x_1} \, \mathrm{d}\xi. \tag{24}$$

The analysis is now limited to positive x_1. The integral in Eq. (24) is evaluated by extending the integrand to complex ξ and in this case by adding a semi-circle of infinite radius in the upper complex half-plane to the path of integration. The complex continuation of the integrand will be an analytical function of ξ for a given ω except at points where the denominator vanishes, i.e. the poles of the integrand. This can be shown using Cramer's rule for solving systems of linear equations (Eq. (17) in this case) and the fact that the sources considered here give components in $\hat{F}^*$ that are polynomials. The contribution from the semi-circle will vanish because of the exponential in the integrand, and therefore the integral is given by a sum of residues of the integrand at the poles,

$$\underset{\sim}{U}^*(x_1, \omega) = \mathrm{i} \sum_p \frac{\underset{\sim}{W}^{\mathrm{T}}_p \hat{F}^*(\xi_p, \omega)}{2\omega c_{gp}} \underset{\sim}{V}_p \mathrm{e}^{\mathrm{i}\xi_p x_1}. \tag{25}$$

The poles, ξ_p, are the values of ξ that for a given ω satisfy the homogeneous version of Eq. (17), $\underset{\sim}{W}_p$ and $\underset{\sim}{V}_p$ are the corresponding left and right eigenvectors and

$$c_{\mathrm{gp}} = \frac{\partial \omega}{\partial \xi} \bigg|_{\xi = \xi_p}. \tag{26}$$

The group velocity, c_{gp}, can be expressed in terms of eigenvectors and matrices as

$$\frac{\partial \omega}{\partial \xi} \bigg|_{\xi = \xi_p} = \frac{1}{2\omega} \underset{\sim}{W}^{\mathrm{T}}_p \big(2\xi_p [K_2] + \mathrm{i}[K_1] \big) \underset{\sim}{V}_p, \tag{27}$$

which is shown by a Taylor expansion of the homogeneous version of Eq. (17), expressing the derivative of the eigenvectors as a sum of the eigenvectors and using relations (21) and (22). Poles on the real axis are included in Eq. (25) only if $c_{\mathrm{gp}} > 0$.

The eigenvalue problem defined in the homogeneous version of Eq. (17) is recast to an ordinary generalized eigenvalue problem in ξ by doubling the size of the matrices, see Kohl et al. (1992b) for example,

$$\left(\begin{bmatrix} [0] & [I] \\ [K_0] - \omega^2[M] & [K_1] \end{bmatrix} - i\xi \begin{bmatrix} [I] & [0] \\ [0] & [K_2] \end{bmatrix} \right) \begin{bmatrix} \underset{\sim}{V} \\ i\xi\underset{\sim}{V} \end{bmatrix} = \begin{bmatrix} \underset{\sim}{0} \\ \underset{\sim}{0} \end{bmatrix}, \tag{28}$$

where [I] is the identity matrix. The properties of this eigenvalue problem is discussed in Kohl et al. (1992b) and the most important ones are restated here. From the symmetry properties of the original problem it follows that, if ξ is a real or imaginary eigenvalue with the eigenvector $\underset{\sim}{V}$, then $-\xi$ is also an eigenvalue with the eigenvector $\underset{\sim}{W}$. If ξ is a complex eigenvalue with the eigenvector $\underset{\sim}{V}$, then so are $-\xi$, $\bar{\xi}$ and $-\bar{\xi}$ with eigenvectors $\underset{\sim}{W}$, $\underset{\sim}{\bar{W}}$ and $\underset{\sim}{\bar{V}}$, respectively. The overbar signifies complex conjugation. These properties are useful in computations since both right and left eigenvectors are needed, and it is often more efficient to compute extra eigenvalues (in this case those in the lower half-plane) than to solve two eigenvalue problems.

The spectrum given by Eq. (25) is evaluated for discrete values of ω, where the maximum value, ω_{max}, defines the maximum frequency considered, corresponding physically to a maximum frequency in a low-pass filter. In general there will be $6N$ poles or eigenvalues for a given ω. It is unrealistic to compute all eigenvalues so a truncation, or filtering in ξ, is needed. For large enough values of x_1 the contribution from poles with imaginary parts larger than a given value will be negligible. Removal of poles with real parts larger than a certain value corresponds physically to a receiver with a limited wavelength resolution. For a transducer, for example, this is connected to its physical dimensions. In reality there is also material damping and short wavelengths will be damped more with distance than long wavelengths. Given the spectrum, the time signal, $\underset{\sim}{U}$, is computed using FFT.

4. Examples

Consider a symmetric cross-ply laminate ([90/0$_2$/90]) with material properties according to Table 1, and a width to thickness ratio of 10. Owing to the symmetry of the cross-section the modes of vibration can be divided into four classes, based on whether they are symmetric or anti-symmetric with respect to the two- and three-coordinates. The four different classes are referred to by the displacement characteristic of the lowest mode. Hence, the modes that are symmetric with respect to both coordinates are called extensional modes here. The modes referred to as compliant flexure modes are symmetric with respect to the two-coordinate and antisymmetric with respect to the three-coordinate, and vice versa for the stiff flexure modes. The torsional modes, finally, are antisymmetric with respect to both coordinates. These symmetry properties are used as boundary conditions to reduce the size of the finite element model when solving the eigenvalue problem given by the homogeneous version of Eq. (17).

One-fourth of the cross-section was divided into rectangular planar nine-node Lagrange elements with the same aspect ratio as the cross-section. Satisfying convergence (less than 5% error in the components of $\hat{\underset{\sim}{U}}^*$) was achieved by using a total of 64 elements. All computations were performed in MATLAB (Trademark of Mathworks Inc.) using the built-in routine for eigenvalue extraction for sparse matrices. After computation of the eigenvalues and eigenvectors the symmetry properties were used to translate the

Table 1
Properties of the glass fiber reinforced epoxy ply

E_L (GPa)	E_T (GPa)	v_{LT}	v_{TT}	G_{LT} (GPa)	ρ (kg/m^3)
46	18	0.29	0.42	7.9	1930

eigenvectors for one quarter of the cross-section to eigenvectors for the whole cross-section. These eigen-vectors were then used in Eq. (23) together with the transformed consistent nodal forces $\hat{F}^*$.

Figs. 2–5 show dispersion curves for the compliant flexure, stiff flexure, extensional and torsional modes, respectively. The diagrams labeled *a* show circular frequency against both real, imaginary (solid lines) and
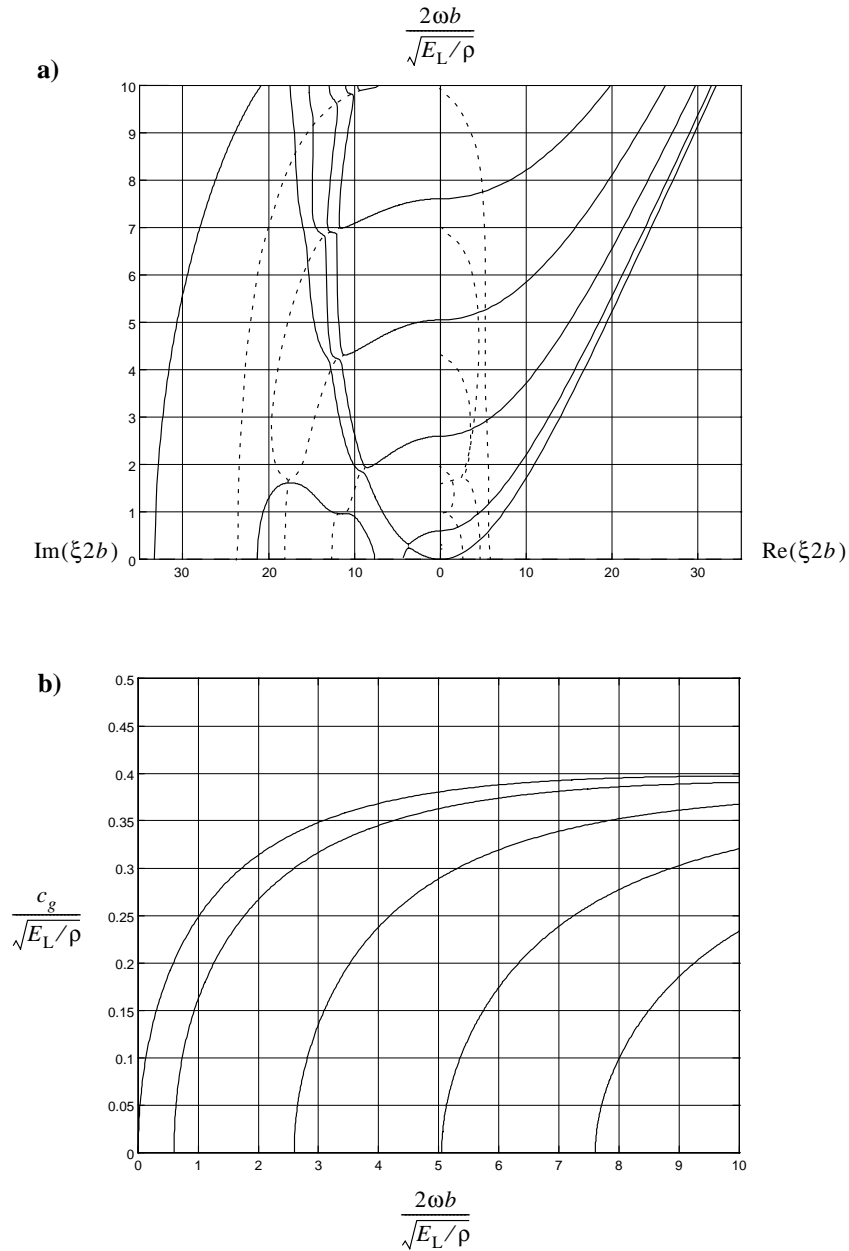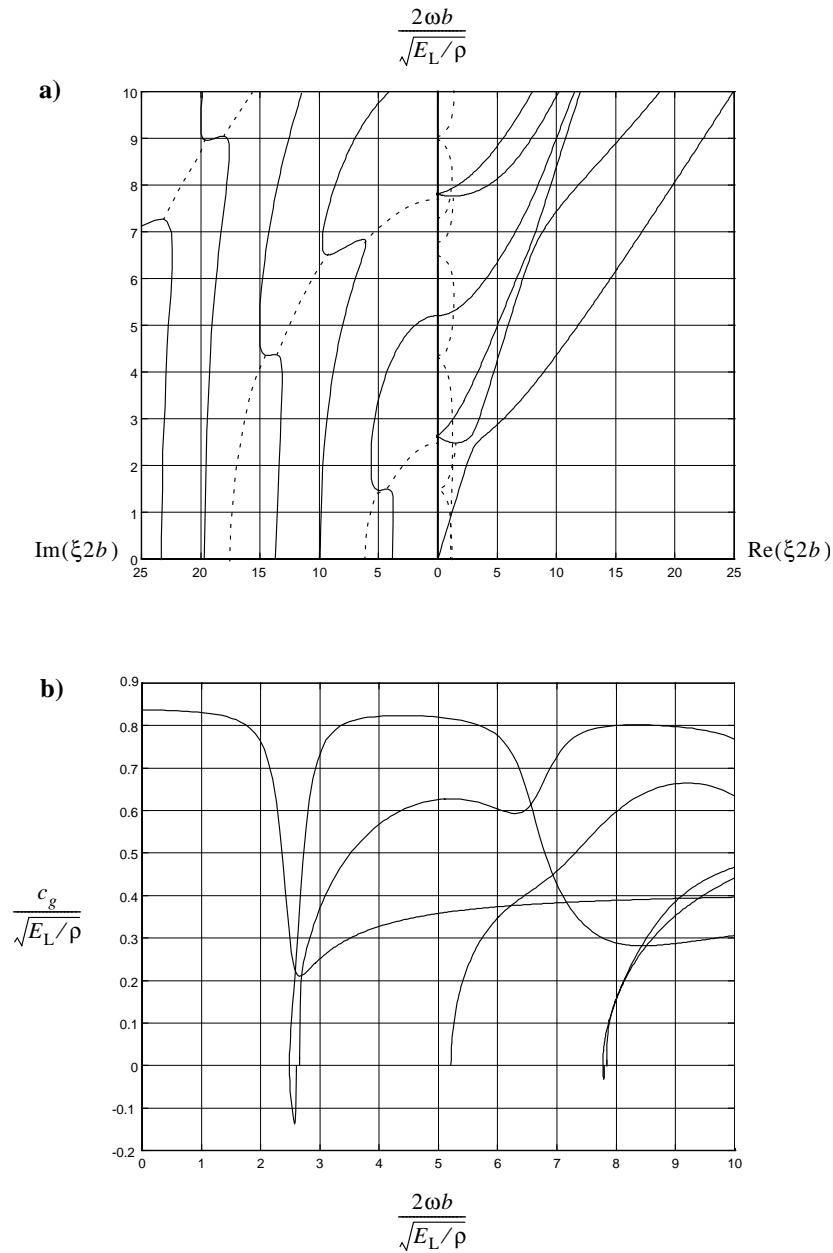

Fig. 2. Dispersion curves for the compliant flexure modes: (a) Circular frequency against real, imaginary (—) and projected complex (- - -) wave numbers. (b) Group velocity for the propagating waves versus circular frequency.
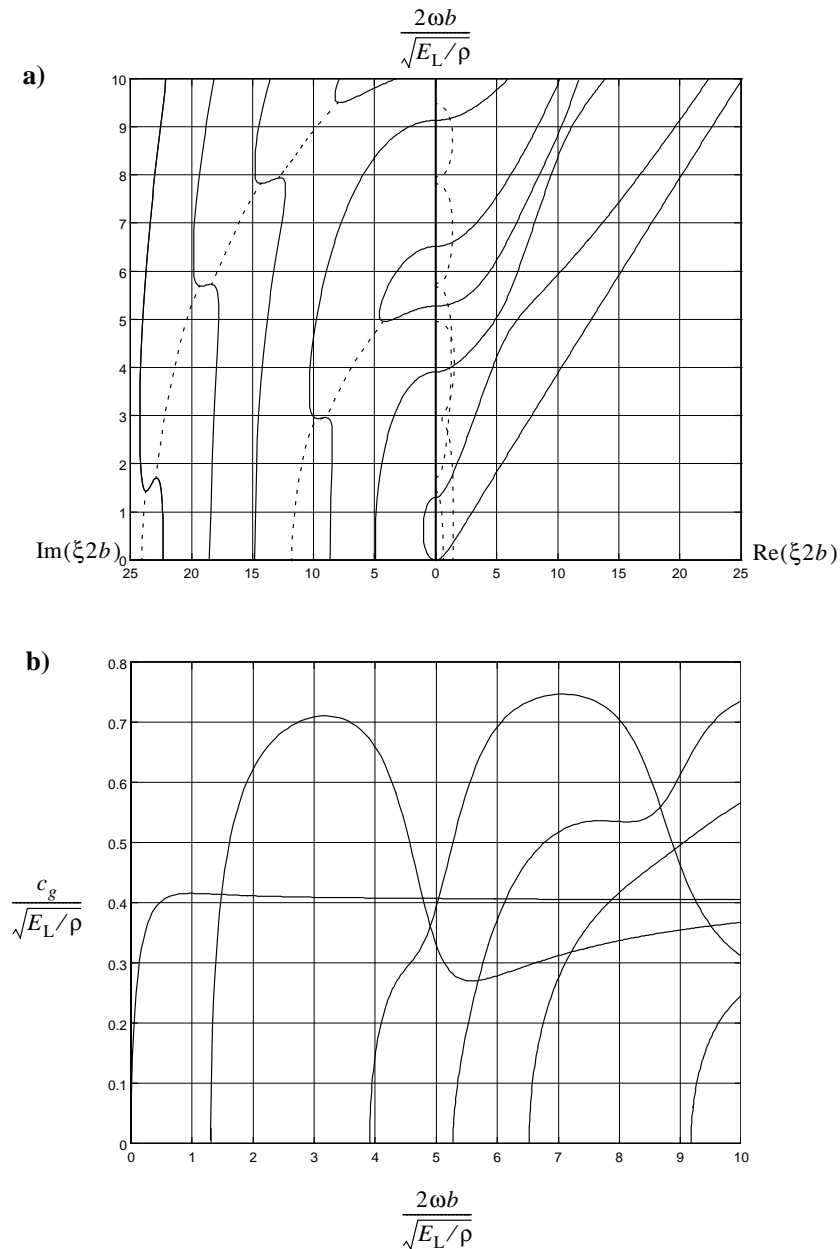
Fig. 3. Dispersion curves for the stiff flexure modes: (a) Circular frequency against real, imaginary (——) and projected complex (- - -) wave numbers. (b) Group velocity for the propagating waves versus circular frequency.

complex (dashed) wave numbers. Real and complex wave numbers are increasing to the right and left respectively, and the real and imaginary parts of complex wave numbers are projected accordingly. The diagrams labeled b show group velocity for the propagating waves (i.e. real wave numbers) versus circular frequency.

$$\frac{2\omega b}{\sqrt{E_L/\rho}}$$

a)

Im($\xi 2b$)   Re($\xi 2b$)

b)

$$\frac{c_g}{\sqrt{E_L/\rho}}$$
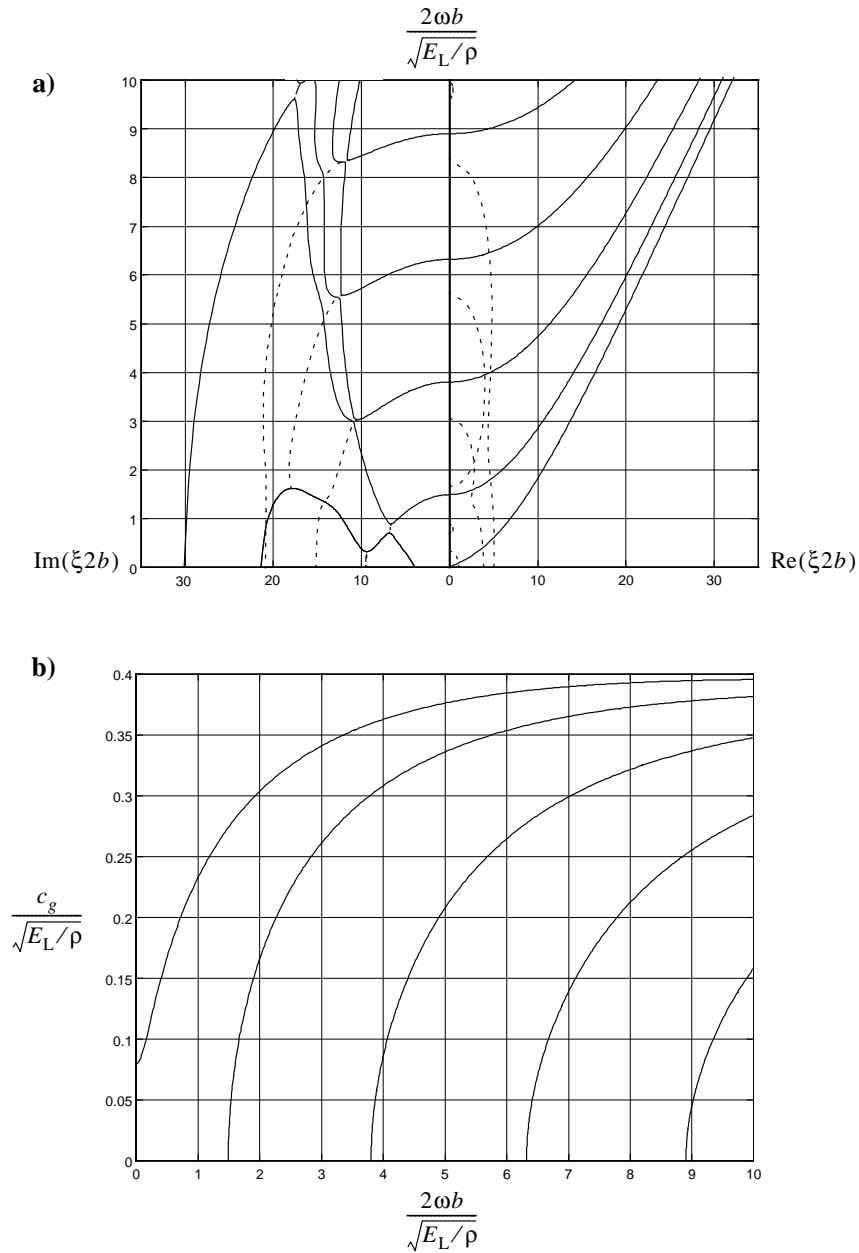
$$\frac{2\omega b}{\sqrt{E_L/\rho}}$$

Fig. 4. Dispersion curves for the Extensional modes: (a) Circular frequency against real, imaginary (—) and projected complex (- - -) wave numbers. (b) Group velocity for the propagating waves versus circular frequency.

4.1. Matrix cracking

The consistent nodal forces describing matrix cracking are integrated from the volume forces given by Eq. (3) and the basis functions. The specimen is assumed to be loaded to a strain $\bar{\varepsilon}_1$ in the 1-direction, which

$$\frac{2\omega b}{\sqrt{E_{\mathrm{L}}/\rho}}$$

a)

$\mathrm{Im}(\xi 2b)$ $\mathrm{Re}(\xi 2b)$

b)

$$\frac{c_g}{\sqrt{E_{\mathrm{L}}/\rho}}$$

$$\frac{2\omega b}{\sqrt{E_{\mathrm{L}}/\rho}}$$

Fig. 5. Dispersion curves for the torsional modes: (a) Circular frequency against real, imaginary (—) and projected complex (- - -) wave numbers. (b) Group velocity for the propagating waves versus circular frequency.

is set to 0.6% in accordance with experiments on the material (Adolfsson and Gudmundson, 1999). Disregarding edge effects, this strain gives the following stress in the 90°-plies

$$\bar{\sigma}_1^{90°} = \frac{E_{\mathrm{L}}^2 E_{\mathrm{T}} + (1 - 2v_{\mathrm{LT}}^2)E_{\mathrm{L}}E_{\mathrm{T}}^2}{(E_{\mathrm{L}} - E_{\mathrm{T}}v_{\mathrm{LT}}^2)(E_{\mathrm{L}} + E_{\mathrm{T}})} \bar{\varepsilon}_1. \tag{29}$$

The static crack opening displacement can be estimated using the fact that the specimen is much wider than it is thick. The crack is thus in a state of generalized plane strain. Referring back to the discussion in Section 2.1 the static crack opening of the surface crack is taken to be, Wu and Carlsson (1991),

$$\Delta u^{\text{stat}}(\eta) = \frac{h}{\sqrt{2}} \frac{(1 - v_{\text{TT}}^2)}{E_{\text{T}}} \bar{\sigma}_1^{90°} \sqrt{\eta}(\alpha_1 + \alpha_2\eta + \alpha_3\eta^2 + \alpha_4\eta^3), \tag{30}$$

where the dimensionless coordinate η is defined by the relation

$$x_3 = \frac{h}{2}(\eta + 1), \quad \frac{h}{2} \leqslant x_3 \leqslant h \tag{31}$$

and

$$\alpha_1 = 4.486, \qquad \alpha_2 = -0.7635, \qquad \alpha_3 = 0.3453, \qquad \alpha_4 = 0.0456. \tag{32}$$

In Eq. (2), the time dependent part of the matrix crack source, the crack propagation velocity was set to $v = 0.1(E_{\text{L}}/\rho)^{1/2}$, which translates to 488 m/s for the material. In addition to the internal volume forces there are non-zero surface tractions, s_i, where the crack extends to the surface of the specimen. In this case

$$\begin{aligned} s_2 &= -C_{1122}\Delta u^{\text{stat}}(x_3)\delta(x_1)J_{\text{m}}(-b, t) \quad t > 0, \ x_2 = -b \\ s_2 &= C_{1122}\Delta u^{\text{stat}}(x_3)\delta(x_1)J_{\text{m}}(b, t) \quad t > 2b/v, \ x_2 = b \end{aligned} \tag{33}$$

and

$$s_3 = C_{1133}\Delta u^{\text{stat}}(h)\delta(x_1)J_{\text{m}}(x_2, t) \quad x_3 = h. \tag{34}$$

In computing the nodal forces, $\underset{\sim}{F}_i$, the surface tractions can be treated in the same way as the volume forces.

Expression (25) was evaluated up to $\omega_{\text{max}} = 10(E_{\text{L}}/\rho)^{1/2}(2b)^{-1}$ with a resolution of $\omega_{\text{max}}/500$. The eigenvalues with the smallest magnitude were computed, and the number of computed eigenvalues increased with frequency from 16 to 32 to assure that no real eigenvalues were excluded. The excluded eigenvalues had imaginary parts of at least $5 \times 2b$, so their influence in the computations was several orders less than numerical inaccuracies. The resulting spectrum for positive ω was then expanded to include negative ω by complex conjugation. Finally, this spectrum of 1001 values was inverted using MATLAB's FFT algorithm.

Figs. 6–9a and b show the velocity due to matrix cracking in the, for AE application most important, 3-direction. The velocities are evaluated at $x_2 = b/2$, $x_3 = h$ and (a) $x_1 = 5b$ and (b) $x_1 = 10b$. Figs. 6–9 show compliant flexure, stiff flexure, extensional and torsional modes, respectively. Velocity in the 2-direction for stiff flexure modes is shown in the Fig. 10a and b. All the velocity components for the extensional mode is shown in Fig. 11. In all cases the signal was subjected to a fifth order Butterworth filter. This was done with the filter routines in the MATLAB signal processing toolbox. The cut-off frequency was set to $9(E_{\text{L}}/\rho)^{1/2}(2b)^{-1}$, giving the frequency response shown in Fig. 12.

4.2. Fiber fracture

The volume forces given by Eq. (4) are integrated to get the nodal forces $\underset{\sim}{F}$. The assumed properties of the glass fibers and the epoxy matrix are given in Table 2. Using the rule of mixtures, see for example
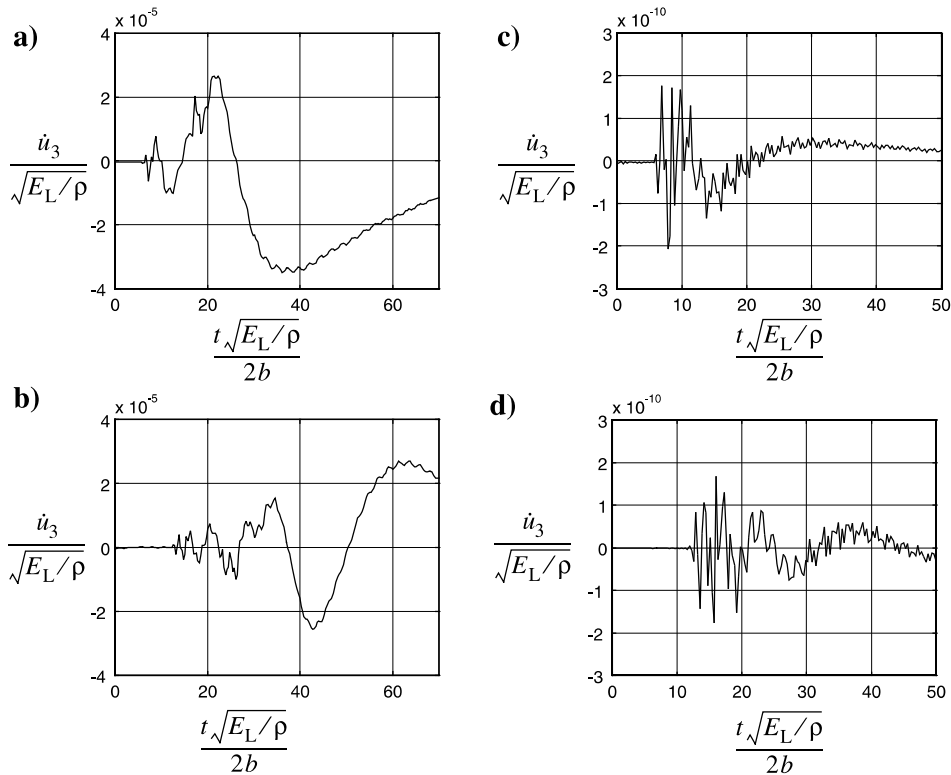
Fig. 6. Velocity in the 3-direction for the compliant flexure modes at $x_2 = b/2$, $x_3 = h$ and $x_1 = 5b$ (a and c) or $x_1 = 10b$ (b and d), due to matrix cracking (a and b) and fiber fracture (c and d).

Gibson (1994), and the known value of longitudinal modulus, E_L, or the density, ρ, the values of Table 2 give the fiber volume fraction, $V_f = 0.6$. The ratio between fiber diameter and specimen width was set to a typical value, $r/b = 5 \times 10^{-4}$. In order to excite all types of modes the position of the fiber fracture was set to $h_f = h/4$, $b_f = b/2$. The strain, $\bar{\varepsilon}_1$, was assumed to have the value 2%. It was also assumed that the fracture takes place during the time $\tau = 2r/(E_f/\rho_f)^{1/2}$. The same frequency resolution, filter etc. as for matrix cracking was applied in this case. The velocity response due to fiber fracture is shown in Figs. 6–10c and d. The observation point is also the same as for matrix cracking.

5. Discussion

The model presented for AE contains two parts. The first part is source modeling. A large uncertainty in this is the assumed time dependence, but detailed direct information on the time dependence is hard to obtain because of the small time and length scales involved. More refined techniques for obtaining the static openings could also be used but as discussed below it is not needed for the wavelengths considered.

The wave-propagation model is thought to be very accurate provided that the material is elastic. In reality, however, viscoelastic material behavior can be expected and it can possibly have large effects on the

a)

$$\frac{\dot{u}_3}{\sqrt{E_L/\rho}}$$

$$\frac{t\sqrt{E_L/\rho}}{2b}$$

b)

$$\frac{\dot{u}_3}{\sqrt{E_L/\rho}}$$

$$\frac{t\sqrt{E_L/\rho}}{2b}$$

c)

$$\frac{\dot{u}_3}{\sqrt{E_L/\rho}}$$

$$\frac{t\sqrt{E_L/\rho}}{2b}$$

d)

$$\frac{\dot{u}_3}{\sqrt{E_L/\rho}}$$
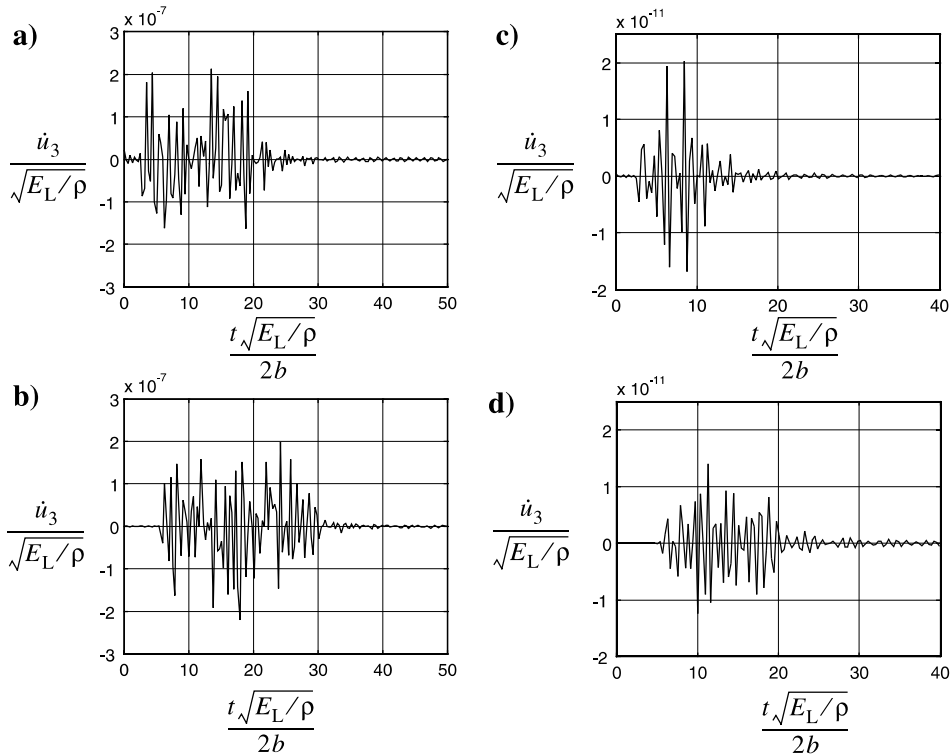
$$\frac{t\sqrt{E_L/\rho}}{2b}$$

Fig. 7. Velocity in the 3-direction for the stiff flexure modes at $x_2 = b/2$, $x_3 = h$ and $x_1 = 5b$ (a and c) or $x_1 = 10b$ (b and d), due to matrix cracking (a and b) and fiber fracture (c and d).

signals. Viscoelastic behavior could, however, be introduced by the use of complex valued stiffnesses, see the work by Mal and Lih (1992).

Looking at the dispersion curves found in Figs. 2a–5a a similarity can be seen between the compliant flexure modes in Fig. 2 and the torsional modes in Fig. 5, and also between the stiff flexure modes in Fig. 3 and the extensional modes in Fig. 4. For the cross-section considered the wave propagation thus seems to be highly dependent on the nature of the symmetry condition with respect to the three-coordinate. A feature seen in the dispersion diagrams is that complex valued branches (dashed) emanate from stationary points on the real or imaginary branches. Furthermore, the optical modes are all stationary at $\xi = 0$. These properties are also found in dispersion diagrams for homogeneous isotropic cylinders and plates as discussed by Onoe et al. (1962) and Mindlin (recited in Miklowitz (1984)). The dispersion curves, especially the complex parts, were in those cases found to be very dependent on the value of Poisson's ratio. A similar behavior can be expected for inhomogeneous waveguides. The complex and imaginary branches, however, have a small influence on the time responses presented. The reason is that for the given values of x_1 the exponential in Eq. (25) becomes very small. The exceptions are poles located close to the real axis for which the slope, or group velocity, tends to be small, which in turn means that the contribution will arrive late in the signal. No filtering in ξ was needed, since all the excluded poles in the computations have large imaginary parts. The maximum value of ξ used for the propagating modes corresponds to a wavelength of $0.36b$. This translates to a little more than two elements per wavelength in the finite element model, which must be considered as a minimum requirement. Also, that the smallest wavelength is 7.2 times larger than
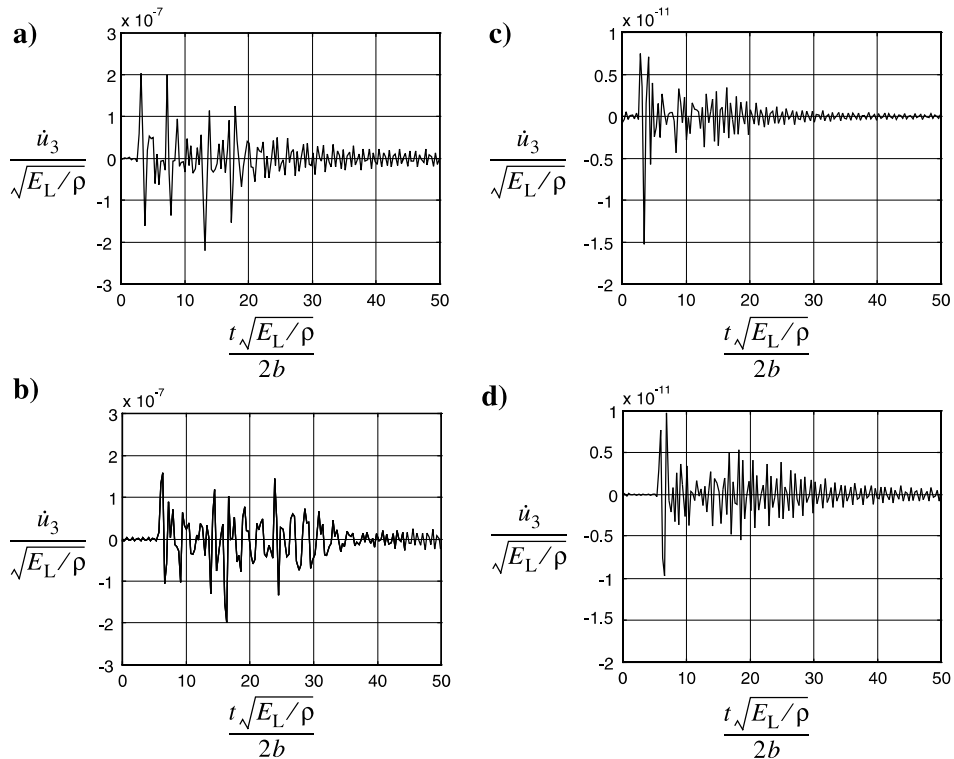
Fig. 8. Velocity in the 3-direction for the extensional modes at $x_2 = b/2$, $x_3 = h$ and $x_1 = 5b$ (a and c) or $x_1 = 10b$ (b and d), due to matrix cracking (a and b) and fiber fracture (c and d).

the height of the matrix crack, which justifies the x_2-dependence assumed for the matrix crack. If smaller wavelengths are desired this dependence has to be modified.

The time histories shown in Figs. 6–11 are not directly comparable to those obtained in AE experiments because the receiving system, especially a transducer, will affect the recorded signal. A transducer will, for example, measure the average signal over the area in contact with the specimen, and the time histories in Figs. 6–11 are due to point values. The averaged response could, however, be synthesized from the point values. Important frequencies in AE experiments on composite specimen are typically less than 500 kHz (de Groot et al., 1995) and the frequency range covered in the computations corresponds to approximately 300 kHz, so this work is potentially useful in interpreting experiments.

A comparison between matrix crack (a and b) and fiber fracture signals (c and d) shows that the former has less high frequency content and longer duration than the latter, as can be expected from the assumed time dependence. The matrix crack signals also have much larger amplitudes than those from fiber fracture, but in reality fiber fracture may involve mechanisms not modeled here. For example, an avalanche of fiber fractures may be triggered by a single fracture resulting in a signal with longer duration and larger amplitude.

Comparing the response for different symmetry classes it is seen that the vertical velocity for the compliant flexure modes and the torsional modes (Figs. 6 and 9) are much larger than the velocity for the stiff flexure and the extensional modes (Figs. 7 and 8). This, however, is highly dependent on the location of the matrix crack or fiber fracture. The vertical velocity due to stiff flexure and extensional modes can to some extent be thought of as lateral contraction velocities. For the stiff flexure modes the largest velocity is in the
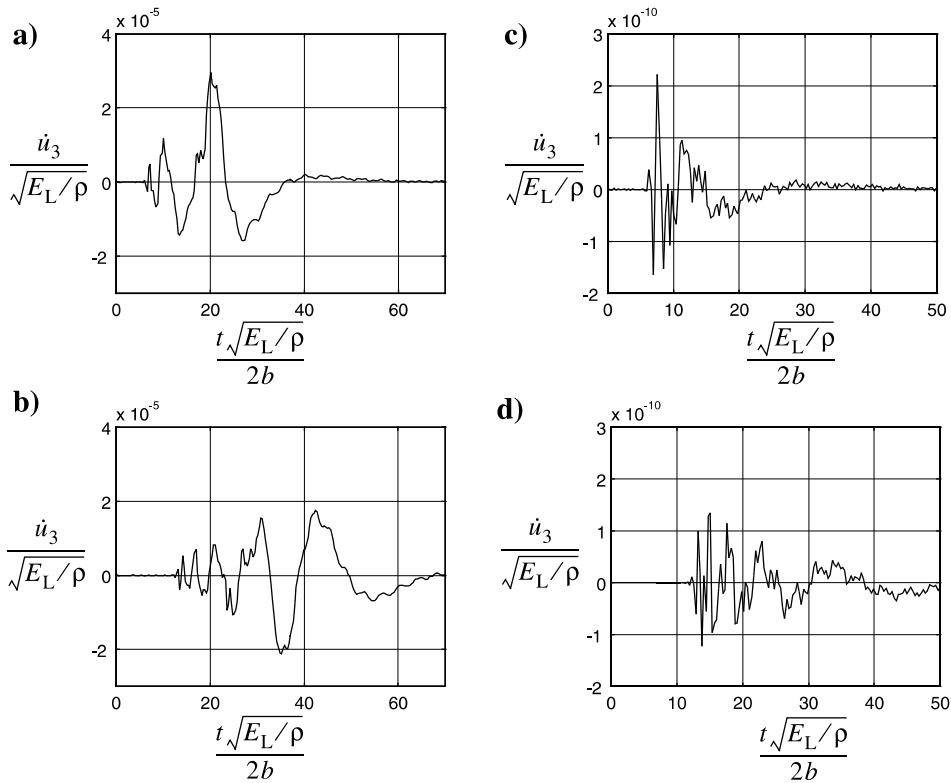
Fig. 9. Velocity in the 3-direction for the torsional modes at $x_2 = b/2$, $x_3 = h$ and $x_1 = 5b$ (a and c) or $x_1 = 10b$ (b and d), due to matrix cracking (a and b) and fiber fracture (c and d).

2-direction (Fig. 10) and for the extensional modes the largest velocity is in the 1-direction (Fig. 11). The duration of the square pulse in the top diagram of Fig. 11 is directly related to the time it takes for the crack to grow across the width of the specimen and so is the distance between the two sharp pulses in the middle diagram.

The response in the vertical direction due to extensional motion, as shown in the bottom diagram in Fig. 11 show four sharp pulses. Two of these, the first and the third, correspond to the negative and positive flanks of the square pulse in the top diagram. These pulses in the vertical response can be seen as lateral contraction due to the square pulse. Lateral contraction is proportional to the strain in the axial direction, or approximately the derivative of the signal with respect to time if dispersion is small. The other two pulses in the vertical direction, the second and fourth, coincide with two pulses in the velocity in the 2-direction. There are two indications that those pulses are due to a wave which, unlike the classical extensional wave, has its main displacement component in the 2-direction. Firstly, the distance between the pulses and the fact that they travel together at a slower velocity than the square pulse seen in the top diagram. Secondly, if the signal is filtered with a low cut-off frequency $(1(E_L/\rho)^{1/2}(2b)^{-1})$ the two pulses disappear. This means that the slower wave is associated with the high frequency content in the signal. Also, looking at the mode shapes it is seen that the lowest extensional mode shifts from having its main component in the 1-direction at low frequencies to having its largest displacement in the 2-direction for higher frequencies. It is possible that the slow wave, visible with high frequency content in the signal, reflects this change, and as is seen from the dispersion curves in Fig. 4 the velocity of the lowest mode is higher for low frequencies than for high
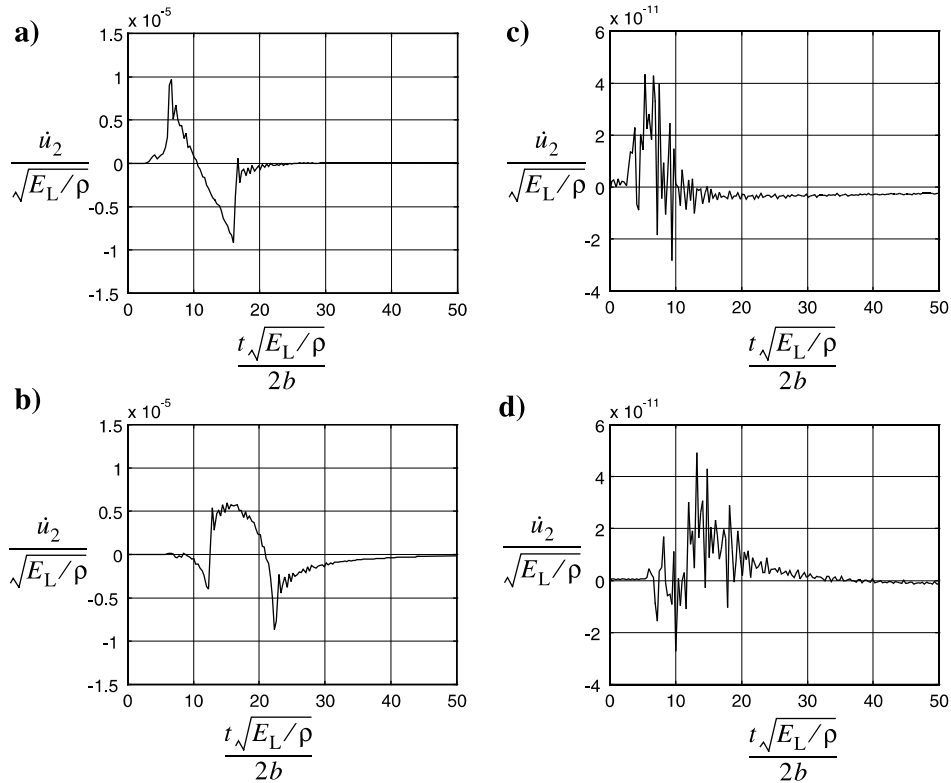
Fig. 10. Velocity in the 2-direction for the stiff flexure modes at $x_2 = b/2$, $x_3 = h$ and $x_1 = 5b$ (a and c) or $x_1 = 10b$ (b and d), due to matrix cracking (a and b) and fiber fracture (c and d).

frequencies. This discussion concerning Fig. 11 illustrates the difficulties in interpreting the AE signals merely in terms of the classical, inherently low frequency, bar and beam extensional and flexural waves. For example, the appearance of the slower wave dominated by motion in the 2-direction cannot be explained in those terms.

The square pulse in the top diagram of Fig. 11 opens a possibility to measure the average velocity of a propagating matrix crack by placing strain gauges in the axial direction. If one gauge is placed on each side of the specimen the interference from Compliant flexure modes can be minimized. The general shape of the square pulse is clearly discernible even if frequencies above $1.5(E_L/\rho)^{1/2}(2b)^{-1}$ are filtered away. For a typical specimen this corresponds to 50 kHz, so the limited band-width of the strain gauges may be sufficient.

Dispersion is evident in all time histories, but is especially marked in the 2-component of the stiff flexure modes, as shown in Fig. 10. Small spurious vibrations before arrival of the real signal as seen in Fig. 8c, for example, are linked to large contributions to the spectrum from poles with very small group velocities. Resolution in ω helps to a point but it is probably more efficient to add a small complex part to ω in the computations as is done in the work by Weaver et al. (1996).

In the previous work (Åberg and Gudmundson, 1999) a higher order beam model described wavemotion, and a maximum frequency of $2.5 \times 2\omega b (E_L/\rho)^{-1/2}$ was used. A comparison of the absolute value and phase of $\dot{U}^*$ from the beam model and the finite element model show that the choice of maximum frequency was justifiable. The main deficiency of the model of Åberg and Gudmundson (1999) was the

(a)

(b)

$$\frac{\dot{u}_1}{\sqrt{E_L/\rho}}$$

$$\frac{\dot{u}_2}{\sqrt{E_L/\rho}}$$

(c)

$$\frac{\dot{u}_3}{\sqrt{E_L/\rho}}$$

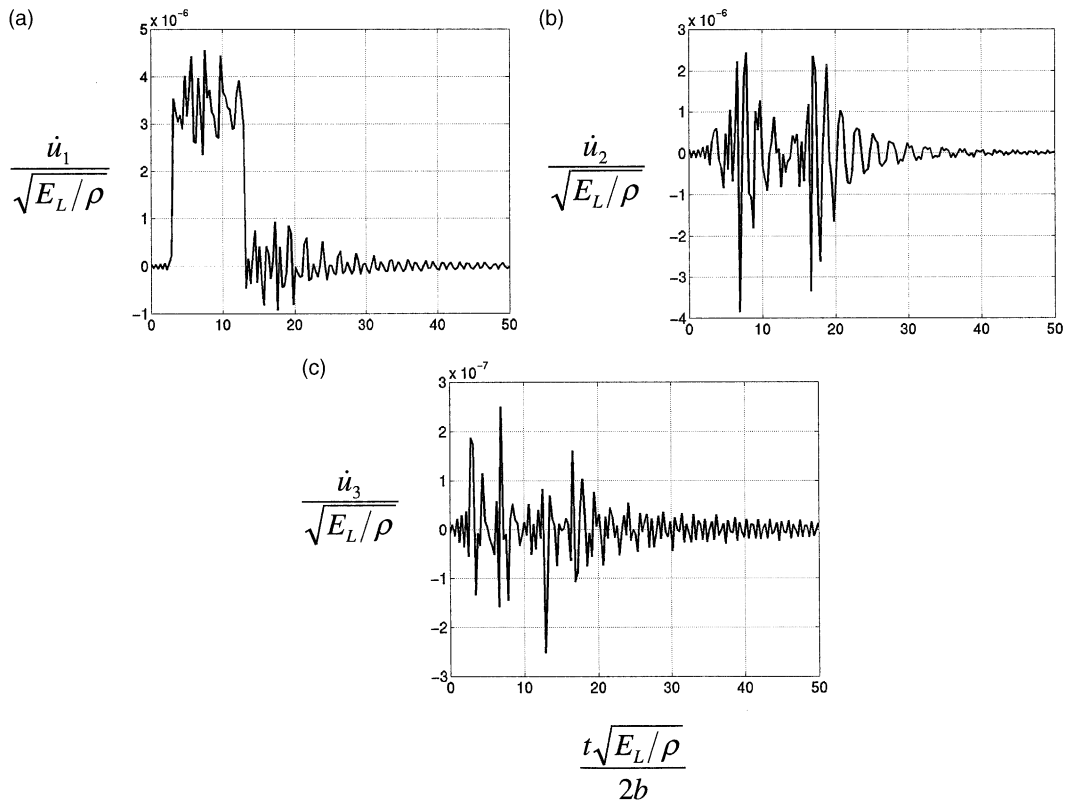$$\frac{t\sqrt{E_L/\rho}}{2b}$$

Fig. 11. Velocity in the 1-, 2- and 3-directions for the extensional modes at $x_2 = b/2$, $x_3 = h$ and $x_1 = 5b$ due to matrix cracking.

neglect of torsional modes. They were not included because it was thought that they would have a small influence on the wave-motion. It is evident from Fig. 9 that this is not the case.

6. Conclusions

With the presented method important AE events such as matrix cracking and fiber fracture can be modeled and relevant frequencies, typically up to 300 kHz, may be included in the resulting wave. There are, however, features not modeled which may prove important, for example material damping. Crucial steps therefore still remain before the results presented herein can be applied directly to AE experiments. The most important is the frequency response of the receiver system.

Judging from the time histories presented, dispersion is a very important phenomenon for wave propagation in tensile test specimen, because it alters the appearance of the signal significantly. It is also seen that the effect of the torsional modes is important. The vertical velocity on the surface of the specimen resulting from matrix cracking is much larger, up to a factor 10^5, than the velocity due to a single fiber fracture. For the geometry studied there is a striking similarity between dispersion curves for compliant flexure modes and torsional modes, and also between extensional and stiff flexure modes.

An experiment to determine the average matrix crack propagation velocity from the low frequency (up to 50 kHz) content in the extensional wave was suggested. The difficulties in explaining the response in terms of classical extensional and flexural beam and bar waves were also illustrated.
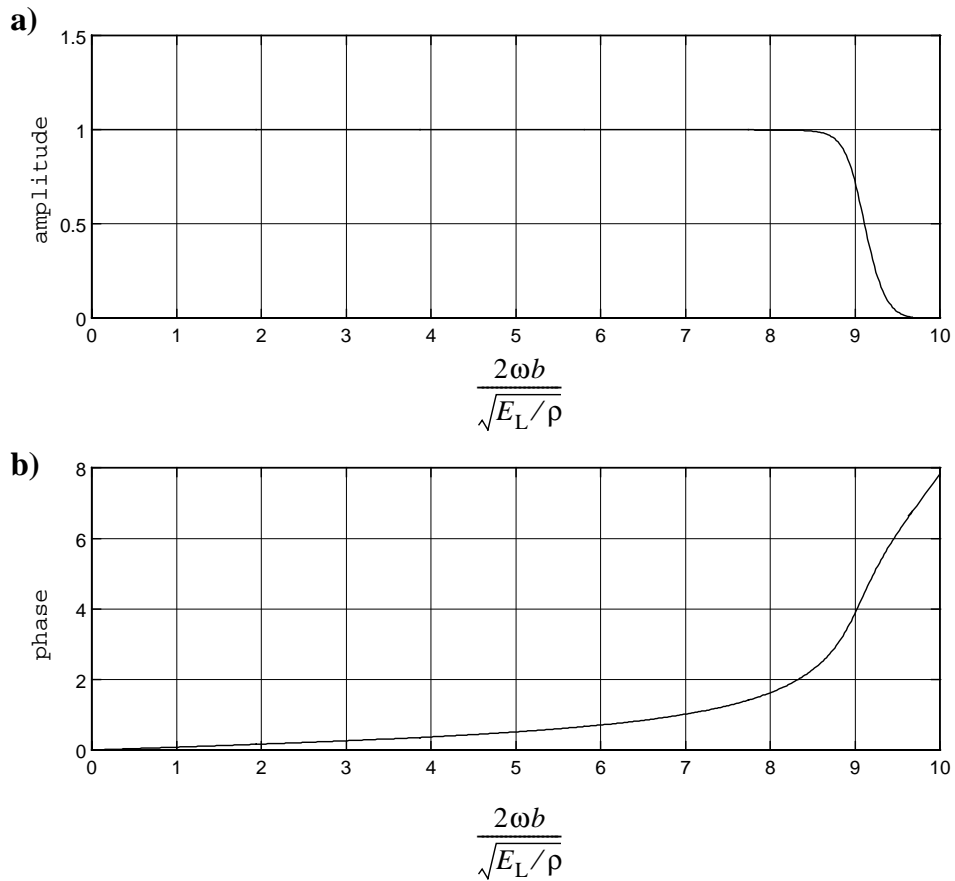
Fig. 12. Frequency response of the fifth order Butterworth filter used.

Table 2
Properties of the glass fiber (f) and the epoxy matrix (m)

E_f (GPa)	v_f	ρ_f (kg/m^3)	E_m (GPa)	v_m	ρ_m (kg/m^3)
73	0.22	2492	4.0	0.35	1120

Acknowledgements

References

Aalami, B., 1973. Waves in prismatic guides of arbitrary cross section. J. Appl. Mech. 40, 1067–1072.
Åberg, M., Gudmundson, P., 1997. The usage of standard finite element codes for computation of dispersion relations in materials with periodic microstructure. J. Acoust. Soc. Am. 102 (4), 2007–2013.

Åberg, M., Gudmundson, P., 1999. Micromechanical modeling of transient waves from matrix cracking and fiber fracture in laminated beams. Int. J. Solids Struct., in press.

Adolfsson, E., Gudmundson, P., 1995. Matrix crack induced stiffness reductions $[(0_m/90_m/ + \theta_p/ - \theta_q)_S]_M$ in composite laminates. Compos. Engng. 5, 107–123.

Adolfsson, E., Gudmundson, P., 1999. Matrix crack initiation and progression in composite laminates subjected to bending and extension. Int. J. Solids Struct. 36 (21), 3131–3169.

Burridge, R., Knopoff, L., 1964. Body force equivalents for seismic dislocations. Bull. Seismol. Soc. Am. 54 (6), 1875–1888.

Chang, C., Sachse, W., 1986. Frequency division method for AE source characterization. J. Acous. Soc. Am. 79 (5), 1307–1316.

Gibson, R.F., 1994. Principles of Composite Material Mechanics. McGraw-Hill, New York.

Gorman, M.R., Ziola, S.M., 1991. Plate waves produced by transverse matrix cracking. Ultrasonics 29, 245–251.

Graff, K.F., 1991. Wave Motion in Elastic Solids. Dover Publications, New York.

de Groot, P.J., Wijnen, P.A.M., Janssen, R.B.F., 1995. Real-time frequency determination of acoustic emission for different fracture mechanisms in carbon/epoxy composites. Compos. Sci. Technol. 55, 405–412.

Gudmundson, P., Zang, W., 1993. An analytical model for thermoelastic properties of composite laminates containing transverse matrix cracks. Int. J. Solids Struct. 30, 3211–3231.

Guo, D., Mal, A., Ono, K., 1996. Wave theory of acoustic emission in composite laminates. J. Acous. Emission 14, S19–S46.

Huang, K.H., Dong, S.B., 1984. Propagating waves and edge vibrations in anisotropic composite cylinders. J. Sound Vibr. 96 (3), 363–379.

Kohl, T., Datta, S.K., Shah, A.H., 1992. Axially symmetric pulse propagation in semi-infinite hollow cylinders. AIAA J. 30 (6), 1617–1624.

Kohl, T., Datta, S.K., Shah, A.H., Rattanawangcharoen, N., 1992. Mode coupling of waves in laminated tubes. J. Compos. Mater. 30 (6), 1617–1624.

Landis, E.N., Shah, S.P., 1993. Recovery of microcrack parameters in mortar using quantitative acoustic emission. J. Nondestr. Eval. 12 (4), 219–232.

Liu, G.R., Tani, J., Watanabe, K., Ohyoshi, T., 1990. A semi-exact method for the propagation of harmonic waves in anisotropic laminated bars of rectangular cross section. Wave Motion 12, 361–371.

Mal, A.K., Lih, S.-S., 1992. Elastodynamic response of a unidirectional composite laminate to concentrated surface loads: Part I. J. Appl. Mech. 59, 879–886.

Miklowitz, J., 1984. The Theory of Elastic Waves and Waveguides. North-Holland, Amsterdam, Netherlands.

Ohtsu, M., 1995. Acoustic emission theory for moment tensor analysis. Res. Nondestr. Eval. 6, 169–184.

Onoe, M., McNiven, H.D., Mindlin, R.D., 1962. Dispersion of axially symmetric waves in elastic rods. J. Appl. Mech. 29, 729–734.

Prosser, W.H., Jackson, K.E., Kellas, S., Smith, B.T., McKeon, J., Friedman, A., 1995. Advanced waveform-based acoustic emission detection of matrix cracking in composites. Mater. Eval. 1052–1058.

Qi, G., Barhorst, A., Hashemi, J., Kamala, G., 1997. Discrete wavelet decomposition of acoustic emission signals from carbon-fiber-reinforced composites. Compos. Sci. Technol. 57, 389–403.

Rice, J.R., 1980. Elastic wave emission from damage processes. J. Nondestr. Eval. 1 (4), 215–223.

Scruby, C.B., 1985. Quantitative acoustic emission techniques. In: Sharpe, R.S. (Ed.), Research Techniques in Non-destructive Testing, vol. 8, pp. 141–210.

Talbot, R.J., Przemieniecki, J.S., 1975. Finite element analysis of frequency spectra for elastic waveguides. Int. J. Solids Struct. 11, 115–138.

Volovoi, V.V., Berdichevsky, V.L., Sutyrin, V.G., 1998. Dynamic dispersion curves for non-homogeneous, anisotropic beams with cross-sections of arbitrary geometry. J. Sound Vibr. 215, 1101–1120.

Weaver, R.L., Sachse, W., Kim, K.Y., 1996. Transient elastic waves in a transversely isotropic plate. J. Appl. Mech. 63, 337–346.

Wu, X.R., Carlsson, A.J., 1991. Weight Functions and Stress Intensity Factor Solutions. Pergamon Press, Oxford, England.